



## Prognosis of COVID-19 Using Ultrasound Scans Augmented by Generative Adversarial Networks

Dasari Naga Vinod<sup>1</sup>    N. Kapileswar<sup>2</sup>    Judy Simon<sup>2\*</sup>    Phani Kumar. P<sup>3</sup>  
 Saraswathy. M<sup>4</sup>

<sup>1</sup>Department of Electronics and Communication Engineering,  
 Vel Tech Rangarajan Dr. Sagunthala R&D Institute of Science and Technology, Chennai, Tamilnadu, India

<sup>2</sup>Department of Electronics and Communication Engineering,  
 SRM Institute of Science and Technology, Ramapuram, Chennai, Tamil Nadu, India

<sup>3</sup>Department of Electronics and Communication Engineering,  
 Chalapathi Institute of Technology, Guntur, Andhra Pradesh, India

<sup>4</sup>Department of Mathematics, SRM Institute of Science and Technology, Ramapuram, Chennai, Tamil Nadu, India

\* Corresponding author's Email: judys@srmist.edu.in

---

**Abstract:** The worldwide problem instigated by multiple mutant forms of the prevalent COVID-19 epidemic; the severe clinical diagnosis remains uncertain. Various clinical prognostic imaging approaches have previously been offered to medical practitioners to identify COVID-19 people. In this article, we introduce a novel diagnostic approach leveraging Generative Adversarial Networks (GAN) and machine learning techniques to enhance the precision and efficiency of COVID-19 diagnosis. Our method integrates advanced image processing algorithms with deep learning models to accurately identify patterns indicative of COVID-19 contamination in medical imaging data. By harnessing the power of GANs, we facilitate the creation of synthetic data for training, thus overcoming limitations posed by sparse datasets. Through rigorous experimentation and validation, we demonstrate the efficacy of our approach in achieving superior diagnostic accuracy compared to existing methods. This research represents a significant advancement in the field of medical imaging diagnostics and holds promise for more effective identification and management of COVID-19 cases. The latter technique supplements Computed Tomography as well as chest X-ray imaging. As a result, utilizing the picture database (7050 Ultrasound Images), our innovative approach utilizes gradient mapping and different haralick characteristics. Distinct techniques were employed to evaluate the classification performance of test sets accompanied by 2110 clinical imaging data. Interestingly, the paper demonstrates that the suggested model's multiple classification accuracy reached 98.1% efficiency among the normal, Pneumonia, as well as COVID-19 by ultrasound image dataset.

**Keywords:** Generative adversarial networks, Gradient mapping, Haralick features, Ultrasound imaging, COVID-19.

---

### 1. Introduction

SARS-CoV-2 has contaminated about 704 million individuals as well as died around 7.2 million (<https://coronavirus.jhu.edu/map.html>). (Accessed on November 24, 2023). Its long and dispersed hatching period necessitates swift, precise, and consistent methodologies for primary ailment diagnosis to effectively combat the contamination [1]. Pre-processing time for the polymerase chain

reaction test (RT-PCR) might be up to one day [2]. Some papers reported accuracy as low as 0.7 [3], while a meta-study estimated the false-negative quantity to be around 0.2 throughout the illness [4]. Medical imaging enhances the analytic cycle, which may govern further PCR testing, especially in emergencies [5]. The optimal imaging level of quality for aspiratory infections is computed tomography (CT) screening [6]. Although an essential evaluation

Table 1. A comparison of chest X-rays, CT scans, as well as ultrasound scans.

Ultrasound	CT scan	Chest X-ray
When the contamination happens in its initial stages, ultrasound can spot pleural as well as interstitial thickening, as well as subpleural consolidation events due to variations in lung erection [12].	CT provides a more realistic way for COVID-19 diagnosis as well as is the most often used diagnostic tool [10, 11].	Chest X-rays are frequently employed to identify lung conditions. In the early stages, they are not well suited to recognize COVID-19 [9].
B-lines are an important phenomenon to diagnose while identifying COVID-19 individuals.	Ground glass opacities (GGO) were reported as bilateral as well as consolidated when COVID-19 individuals were monitored [13].	Patchy, ambiguous bilateral alveolar consolidations with a peripheral distribution are important in identifying COVID-19 patients.
Cheap, easy to sterilize, portable, safe, non-irradiating, as well as widely accessible.	It is extremely radiative, costly, and difficult to sterilize.	Expensive, radiating, and with no statistical significance.

of patients illustrates conventional CT scans, it is deemed reliable for Coronavirus diagnosis in certain countries [7]. Nonetheless, a CT scan is an expensive and extremely revealing procedure that poses a noteworthy risk of cross-contamination to medical practitioners as well as necessitates widespread, time-consuming decontamination [8]. Table 1 shows contrasts of radiography images like CT scans, chest X-rays as well as ultrasound against numerous criteria.

Currently, ultrasound pictures, an extra widely available, cost-effective, secure, as well as consistent imaging technology, have come under scrutiny in the setting of severe respiratory disorders. Lung ultrasonography (LUS) in particular provides enormous advantages in the point-of-care scenario for the detection and management of individuals with severe respiratory disorders [14, 15]. In some instances, it was more effective than a chest X-ray in recognizing pneumonia [16]. Doctors have currently illustrated the use of ultrasound scans in the calamity for the identification of COVID-19-affected individuals [17]. Findings suggest that clear LUS characteristics and imaging biomarkers for COVID-19 individuals [18]-[20] might be used to both identify these individuals and deal with the respiratory adequacy of mechanical ventilation [21]. When individual inflow exceeds the typical medical imaging platform capabilities, ultrasound pictures provide a broad range of suitability and generally lower costs. It is also available to low as well as middle-income Nations [22]. Nonetheless, depicting ultrasound scans may be a difficult chore; also, it leads to inaccuracies due to a high learning curve [23]. This article's most important scientific contributions are as follows:

- Using lung Ultrasound images, we proposed a gradient mapping using the GAN mechanism to distinguish Normal, COVID-19, along Pneumonia persons.
- We thoroughly evaluated the ultrasound image samples used to track Normal, COVID-19, as well as Pneumonia. Qualified radiologists confirmed all of the images including lesions.
- The collected findings were analyzed using three metrics: accuracy, confusion matrix as well as ROC.
- The proposed approach indicated for the current experiment assists in the identification of COVID-19-contaminated samples and acquired an accuracy score of 98%.
- For the approximation analysis, the suggested approach yields 98.1% accuracy.

The remainder of this paper is structured as ensue: The second segment examined the most modern lung ultrasound scans. The picture dataset as well as pre-processing are shown in Section 3. We explained gradient mapping as well as image separation on the image dataset in Section 4. Section 5 depicts the experimental outcomes as well as a discussion of the method's performance, and Section 6 concludes with an epilogue.

## 2. Literature survey

Conventional techniques for diagnosing COVID-19, such as polymerase chain reaction (PCR) testing and radiological imaging, suffer from several limitations that hinder their effectiveness in accurately identifying infected individuals. PCR testing, while considered the gold standard for

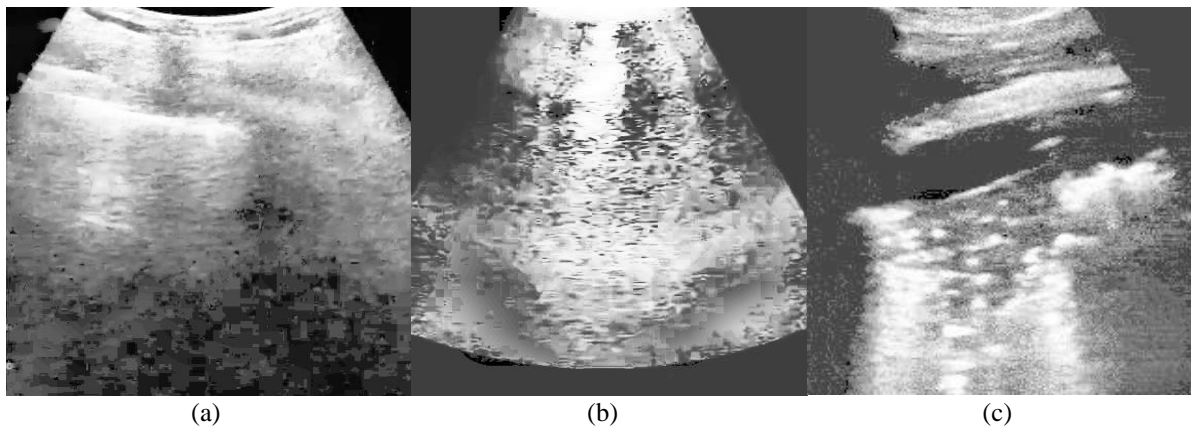


Figure. 1 Database sample lung ultrasound pictures: (a) An example of a COVID-19-contaminated lung with modest subpleural consolidation and pleural abnormalities, (b) A lung that is in good health, and (c) A pneumococcal lung with dynamic air bronchograms surrounded by alveolar consolidation

COVID-19 diagnosis, often requires specialized laboratory equipment, and time-consuming sample processing, and can yield false-negative results, particularly in cases of low viral load or improper sample collection. Radiological imaging methods, including chest X-rays and computed tomography (CT) scans, offer rapid results and visual evidence of lung abnormalities characteristic of COVID-19 pneumonia. However, these imaging modalities are limited by their subjective interpretation, reliance on expert radiologists for analysis, and the potential for variability in image quality and consistency across different healthcare settings. Lung ultrasound (LUS) as shown in Fig. 1 is an imaging method used by doctors at the point of care to help with the identification as well as treatment of acute respiratory failure. In addition to coordinating or outperforming X-rays of the chest for most acute respiratory illnesses, LUS avoids radiation as well as the laborious process of CT [24-26]. Furthermore, as an affordable battery-powered solution, LUS may be disseminated widely in any context and well-suited for pandemic circumstances [27]. B lines are the main features of LUS caused by pulmonary edema or the non-cardiac consequences of interstitial syndromes [28].

Clinical imaging, for example, can play an important role in augmenting classic symptomatic equipment from subatomic research. The authors of [29] demonstrated some programmed techniques employed by ML as well as AI techniques, capable demonstrations using X-ray as well as Computed Tomography data. Furthermore, researchers in [30] presented a POCOVID-Net convolutional neural network to handle present computer vision assistance. It is deduced that using the convolutional component of VGG-16 and creating a deep convolutional neural network successfully impacts multiple picture kinds

[31]. This is accompanied by one hidden layer with 64 cells activated by the ReLU activation function, 0.5 dropouts [32], and group standardization [33]. In 5-fold cross-validation, the model had a grouping precision of 89% as well as an accuracy to identify COVID-19 by 96%. The approach demonstrates the analytic value of the obtained data as well as the applicability of deep learning to ultrasound images.

Born et al. [34] offer a freely accessible Coronavirus LUS database that includes 202 videos from four classifications (Bacterial pneumonia, Coronavirus, non-coronavirus viral pneumonia, as well as typical pictures). In this database, researchers explored the use of ML algorithms for differential diagnosis of lung diseases. In a blinded report with clinical experts, they used interpretability techniques for the Spatiotemporal confinement of pneumonic biomarkers to investigate the usability of the proposed methodology regarded as valuable for human-tuned scenarios. As a result, they suggested a frame-based technique that correctly identifies COVID-19 LUS images from normal along with bacterial pneumonia data, yielding an affectability score of  $0.90 \pm 0.08$  as well as a specificity score of  $0.96 \pm 0.04$ .

Hu, Z. et al. [35] proposed MCRFNet, a unique classification network that arranges lung sonograms using a multimodal combination, channel, along the response field. In addition, the writers assessed the predicted classes that mirror the patient's amount of lung involvement and supported experts in connecting various pointers to survey disease drifts in COVID-19 patients. Roy et al. [36] defined the benchmark condition of ML techniques for analyzing pixel-level identification of COVID-19 image biomarkers. Analyses of the dataset demonstrate a good conclusion on all of the considered chores, paving the way for further research on DL for the

aided detection of Coronavirus using the LUS database [37-40]. Ferhat et al. [42] proposed Transfer Learning positioned CNN recognizing COVID-19 enabled by X-ray films with 75% veracity and an accuracy of 80% for the VGG pre-trained model [43]. In contrast to conventional techniques, our proposed method represents a paradigm shift in COVID-19 diagnosis by leveraging cutting-edge technologies such as Generative Adversarial Networks (GANs) and machine learning algorithms. By integrating GANs with medical imaging data, we address the limitations of sparse datasets by generating synthetic images that enhance the robustness and generalization of our diagnostic model. Additionally, our approach incorporates advanced image processing techniques to extract and analyze subtle patterns indicative of COVID-19 infection, thus enabling more accurate and objective diagnosis compared to traditional radiological interpretation methods.

### 3. Materials and methods

#### 3.1 Preprocessing the database

The group of data utilized in this task is freely accessible in the GitHub database [37] (**Note: IRB approval was not required for this study**), and it contains around 7050 ultrasound images which augments 7050 images in various angles, out of which 2350 COVID-19-positive instances, 2350 normal people, as well as 2350 Pneumonia patients. The image database archive is available for image disjunction approaches, as well as the complete database has been checked and clarified, including the finding of the LUS pictures. Because the images in the collection are not flexible, ultrasound images adequately enunciate the characteristic range; we have changed all of the photos to a comparable dimension of  $512 \times 512$  pixels. Furthermore, RGB reversion has been applied, and the resulting input to the proposed approach is a  $512 * 512 * 3$  image. Following that, we used gradient mapping, as well as GAN to this model along with computed haralick features for both spatial areas (GLDM, GLCM & Texture) with frequency areas (DWT & FFT).

#### 3.2 Feature extraction

Gray-level co-occurrence Matrix (GLCM), Texture, Fast Fourier Transform (FFT), Grey Level Distance Method (GLDM), and Discrete Wavelet Transform (DWT) were used to assess a total of 200 characteristics in both frequency as well as spatial domains. We calculated the 12 Haralick traits as

Vinod et al. [41]. The feature extraction approach yielded almost 200 lineaments for each ultrasound picture (“96 lineaments arising from DWT, 12 lineaments arising from texture as well as FFT separately, 40 features arising from GLCM and GLDM separately”).

#### 3.3 Generative adversarial network

GANs are an element of deep learning models [29]. GANs are a unique form of neural system representation in which two distinct structures are executed concurrently, one focusing on generation while the other discriminating. GANs give an approach to learning deep knowledge in the absence of extensively clarified training data. They learn by calculating inverted spread signals via a competitive approach that involves two networks. Because of its simplicity in dealing with field changes and feasibility in developing new picture sets, this excellent training strategy has piqued the interest of both the scholarly community as well as businesses. GANs have made tremendous progress and are widely utilized in a variety of applications, including picture editing, pattern classification, as well as image synthesis [29].

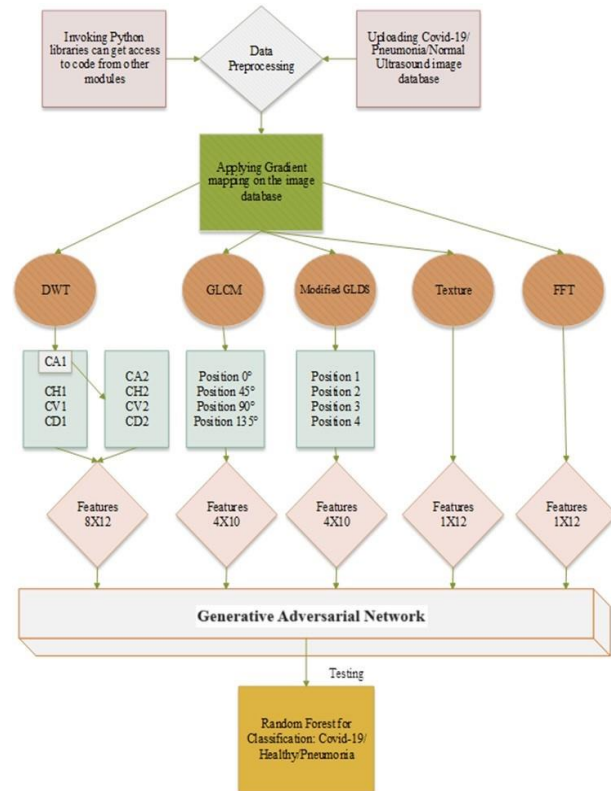


Figure. 2 Recommended approach for identifying normal/pneumonia/COVID-19 patients

#### 4. Suggested approach

To train the large image dataset, the training system employs the “anaconda-Jupyter notebook by tensor flow” approach described by Vinod et al. [41]. Access to the necessary libraries was granted at the outset to link the code from other mechanisms. After that, upload the picture database to the route, then apply gradient mapping to the LUS scans and extract the lineaments using spatial as well as frequency areas such as “GLDM, FFT, DWT, GLCM along with Texture” for segmentation. Lastly, we added all 200 haralick features in both areas and used the Generative Adversarial Network approach aided by the random forest algorithm to determine COVID-19 individuals, as shown in Fig. 2. Mechanism-1 depicts the image pre-processing procedure, whereas mechanism-2 depicts the feature elimination of the images. Finally, mechanism 3 for an LUS picture database with different categories and effectiveness procedures of the system are shown.

---

##### Mechanism 1: LUS films for Pre-processing

---

Input: Input Ultrasound film  $i(a, b, c)$   $(a, b, c) \in (1, 2, \dots, m)^3, a = b = c$   
 Output: Output Ultrasound film  $o(a, b, c)$   $(a, b, c) \in (1, 2, \dots, m)^3, a = b = c$   
 Begin  
 For every Input Ultrasound film,  $i$  proceed  
 For  $\{a, b, c\} = 1$  to  $m$  proceed  
 Enforce gradient mapping for generating the heat maps by Eq. (5) on the films  
 Transform input film  $i$  into gray as well as resize the film by  $512 \times 512$   
 Enforce min-max normalization as well as revert the output film( $o$ )  
 End For  
 End For

---

Here  $a$ ,  $b$ , and  $c$  are the classes in the ultrasound films and  $m$  is the quantity of films.

---

##### Mechanism 2: LUS films for Feature Extraction

---

Input: Input Ultrasound film  $o(a, b, c)$   $(a, b, c) \in (1, 2, \dots, m)^3, a = b = c$   
 Enforcing GAN  
 Begin  
 For each Input Ultrasound film  $o$ , proceed  
 For  $\{a, b, c\} = 1$  to  $m$  proceed  
 If file  $\leftarrow a$ , Then  
 Class  $\leftarrow 0$   
 ELIF file  $\leftarrow b$ ,  
 Class  $\leftarrow 1$   
 ELSE

Class  $\leftarrow 2$   
 ENDIF  
 End For  
 End For  
 $G \leftarrow \{\text{Determining lineaments on input ultrasound films } o \text{ (12 lineaments)}\}$   
 Textual,  $l \leftarrow \text{Calculate } G \text{ on the input ultrasound films, } o$   
 FFT,  $f \leftarrow \text{Calculate } G \text{ on the input ultrasound films, } o$   
 DWT,  $t1 \leftarrow \text{Calculate } G \text{ on the input ultrasound films, } o$   
 DWT,  $t2 \leftarrow \text{Calculate } G \text{ on Approximation of } d1 \text{ image}$   
 $T \leftarrow t1 + t2$   
 GLDM,  $D \leftarrow \text{Calculate } G \text{ on input ultrasound films } o \text{ in 4 aspects by Eq. (6)}$   
 GLCM,  $M \leftarrow \text{Calculate } G \text{ on input ultrasound films } o \text{ in 4 aspects}$   
 Ultra Covix mechanism  $\leftarrow \sum_{i=1}^m \{l, f, T, D, M\} \in o$   
 (Total  $G=200$ )  
 Save the mechanism

---



---

##### Mechanism 3: Build the LUS films employed by the Ultra Covix mechanism

---

Input: Ultra Covix mechanism, number of instances = 100, Training ratio = 70%, Testing ratio = 30%, Classifier = Random Forest, number of trees = 100.  
 Output: Visualization, Confusion Matrix, Training, Performance accomplishment, as well as accuracy loss.  
 Begin  
 For the Input Ultra Covix mechanism, proceed  
 $x = \text{concatenate } \{(a(G), b(G), c(G))\} \in (1, 2, \dots, m)^3 \text{ (inputs)}$   
 $y = \text{concatenate } \{(a(G), b(G), c(G))\} \in (1, 2, \dots, m)^3 \text{ (target class)}$   
 End For

---

#### 4.1 Gradient mapping

Gradient translation is a prominent mode. It explains that it uses extensive average pooling as well as allows for the estimation of class-specific heat maps that indicate the discriminative parts of the picture that elicit suitable class activity of interest [38]. Gradient technique based on the basic assumption that the final count  $X^d$  for a given category  $d$  may be shown as a linear combination of its extensive average pooling last convolutional layer feature mappings  $B^i$ .

$$X^d = \sum_i g_i^d \cdot \sum_m \sum_n B_{mn}^i \quad (1)$$

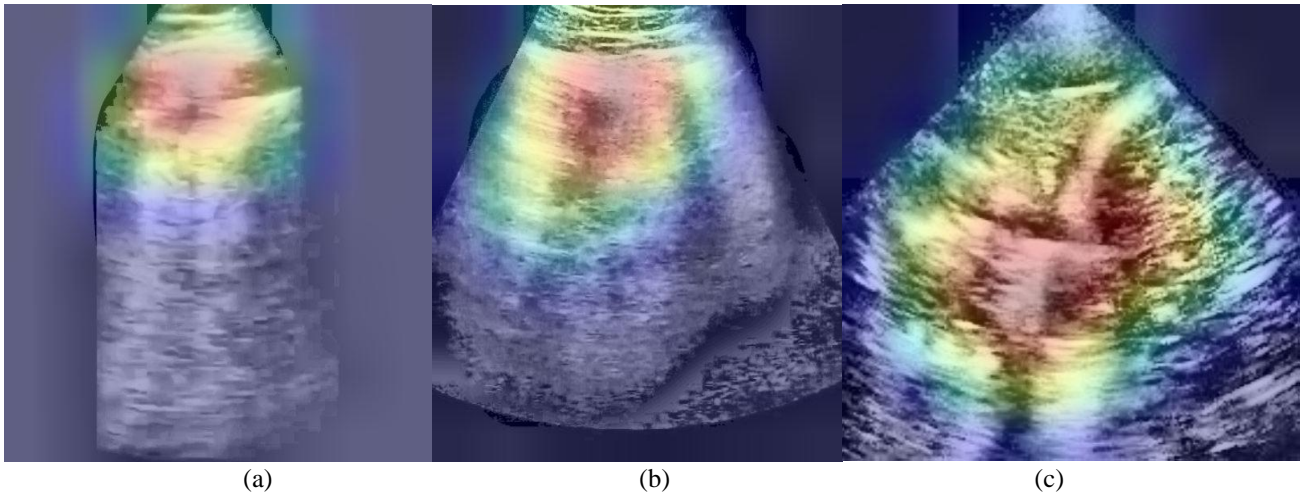


Figure. 3: (a) COVID-19 gradient mapping sample image (highlighted B-line), (b) normal (highlighted A-lines), and (c) Pneumonia (highlighted Pleural consolidations).

Respective spatial location  $(m, n)$  in the category-specific saliency map  $S^d$  is then estimated as:

$$S_{mn}^d = \sum_i g_i^d \cdot B_{mn}^i \quad (2)$$

$S_{mn}^d$ , precisely associated with the significance of a specific spatial location  $(m, n)$  for a particular class  $d$  as well as thus aims as perceptible data of the category foreseen by the network. The label activation map assesses these weights  $g_i^d$  by training a linear classifier for each group  $d$  using the activation maps of the last convolutional layer skillful for a given image, the weights  $g_i^d$  for a suitable feature map  $B^i$  and the group  $d$  is corresponding to:

$$g_i^d = Y \cdot \frac{\partial X^d}{\partial B_{mn}^i} \quad \forall \{m, n \mid m, n \in B^i\} \quad (3)$$

Here  $Y$  is fixed, exploiting gradients flowing from the output class into activation maps of the last convolutional layer as neuron importance weights  $g_i^d$ .

$$g_i^d = \frac{1}{Y} \sum_m \sum_n \frac{\partial X^d}{\partial B_{mn}^i} \quad (4)$$

The label selective saliency maps for a given image,  $S^d$  are then assessed as a linear combination of the forward activation maps, followed by a ReLU activation function. Each spatial feature in the saliency map  $S^d$  is then intended as:

$$S_{mn}^d = \text{ReLU}(\sum_i g_i^d \cdot B_{mn}^i) \quad (5)$$

Gradient mapping or its hypothesis for medical purposes Grad-CAMs [39] can provide appropriate decision assistance by interpreting either a system that detects its placement on exact pathological

measures or an algorithm that recognizes its location on specific pathological measures. Gradient mapping can also advise healthcare professionals as well as point to descriptive arrangements, which are particularly suitable for time-sensitive or insight-sensitive situations. To diagnose COVID-19 individuals, the gradient picturing provides numerous dissection methods such as Texture, FFT, GLCM, Wavelet & GLDM that identify distinct diagnostic methods, and conclusions were initiated better performance by observation.

The gradient mapping approach is shown in Fig. 3 on lung ultrasound scans with and without COVID-19. We determined the point's maximal activation of the gradient translation of every category (Pneumonia, Normal & COVID-19) along with all image datasets for a more visual evaluation. While the heat maps are evenly distributed around the probe, pneumonia-associated characteristics, which are particularly connected to COVID-19 as well as Normal patterns, are concentrated at the center and bottom.

#### 4.2 Segmentation based on FFT

The Fast Fourier Transform (FFT) measures the inverse of the discrete Fourier Transform (DFT). The FFT expansion is employed to novitiate a digital signal  $(d)$  among range  $(r)$  from the time region into a recurrence district  $(R)$ , taking into account the amplitude of vibration based on its stimulating within the recurrence as the sign emerges.

To robotize the decision-making procedure for the susceptible frequencies to the defect under examination, the periodicity range vector is divided into distinct frequencies. The normal of each degree is then used as a physical perspective for the material.

We identified the 12 quantifiable aspects of the FFT in all ultrasound scans.

### 4.3 GLCM-based segmentation

The Grey Level Co-occurrence Framework is a scientific cycle that is widely used to depict images, most notably for Second Harmonic Generation (SHG) collagen image categorization. This paradigm considers the spatial relationship of picture pixels at a given position. It is typically approximated for all four directions at a specified range. A textural characteristic persists across this lattice. Different directions are frequently discriminated or identified in the center value to get an initial estimation limit.

Officially, the co-occurrence lattice is defined as the probability of a grey level  $p$  occurring in the vicinity of another grey level  $q$  at an offset  $f$  in course  $C$ ,  $S(p, q | f, C)$ , wherein  $f$  is a removal vector,  $f = (\Delta c, \Delta i)$ .  $C$  is one of the eight possible directions. The difference between reverse directions is usually ignored, and symmetric probability lattices can thus be used specifically for four aspects ( $135^\circ$ ,  $90^\circ$ ,  $45^\circ$ , &  $0^\circ$ ). Image features are extracted from this lattice using accurate estimates. We established the first 10 quantifiable requirements in four spatial regions for full images in GLCM.

### 4.4 Segmentation based on texture & GLDM

Texture as a picture attribute is extremely important in many image management applications, as well as in applications that use computer vision. In the picture refining investigation, a comprehensive look at surface evaluation revealed the essential focus on hand, division, as well as association. Surface characteristics have been employed in a variety of applications, including satellite and aeronautical image evaluation, clinical image inspection for distinguishing variations from abnormalities, and, most recently, image recovery utilizing the surface as a descriptor. This section describes a method for representing the surface utilizing a multi-band image degradation with applications to depiction, segmentation, object recognition, and image recovery. We identified the twelve factual components from each of the images during the surface assessment.

The grey level difference technique thickness capacity about the pre-handled grey image. This method is used to remove all surface characteristics from a high-level image. Contrast is defined as the difference in thickness between the most important and least important layers in a photograph. As a result, the local ranges are on the grey scale. We computed the first ten quantifiable features in four spatial regions between range,  $r = 8$ , in overall images in the

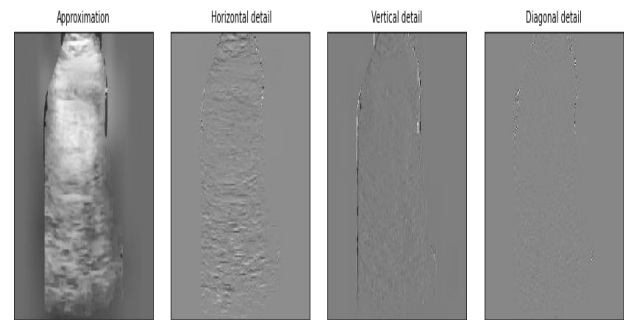


Figure. 4 Wavelet transform technique on the Ultrasound slices of COVID-19

data set using reference and neighbor pixels  $(x, y)$ .

$$J(x, y) = |I(x, y) - I(x, y + r)| \quad (6)$$

Here  $I$  is the input image.  $J$  is the output of image  $I$ , and  $r$  is the GLDM estimate distance.

### 4.5 Segmentation based on wavelets

A discrete wavelet transform (DWT) is always represented as a non-excess attempted CWT. The wavelet transformation seeks to surround a discrete-time plan,  $x(s)$ , with as many (wavelet) coefficients as possible. These coefficients are often assessed using a CWT to establish a balanced set of tolerable bounds. Wavelet configurations abound, with varying properties. This section, however, is limited to the case of even wavelets with little aid.

The wavelet may be viewed from a handful of different perspectives. In this case, we'll look at the wavelet via the lens of a channel bank. There are a few finite impulse response (FIR) channels containing  $N$  coefficients shown. One of these channels is high-pass, whilst the other is low-pass; the two channels cut on/off at various points throughout the examination repetition. These channels, as well as their recursive use, may be used to define the wavelet transform. The channels are initially applied to the input time course of action to generate distinct low-pass as well as high-pass sections,  $X_1(s)$  and  $X_2(s)$ :

$$X_1(s) = \sum_{l=0}^{N-1} e_l y(s - l) \quad (7)$$

$$X_2(s) = \sum_{l=0}^{N-1} f_l y(s - l) \quad (8)$$

Here  $e_l$ , and  $f_l$ , are the low-pass as well as high-pass filter coefficients separately. It is completely normal to construct the high-pass channel before the low-pass channel, which is extensively adapted utilizing the turning flip arrangement, thus the two designs of channel coefficients are related through:

$$f_l = (-1)^l e_{M-l} \quad (9)$$

The yield of the two filters is a significant portion of the input progression transmission capacity, so  $X_1(s)$  contains the lower band, and  $X_2(s)$  includes the higher band. The yields of each channel are a high ratio of the initial data transmission of  $X(s)$  to give these double cross designs containing massive data.

As indicated in Fig. 4, we used two-way sequential coefficient functions such as (Coefficient Approximation) CA1, (Coefficient Horizontal) CH1, (Coefficient Vertical) CV1, and (Coefficient Diagonal) CD1. CA1 identified more wavelet coefficients repeatedly; for example, CA2, CH2, CV2, and CD2 for each consecutive coefficient, we determined the twelve factual characteristics.

#### 4.6 Applying the random forest technique

Random Forest is a supervised learning approach that may be used to solve classification and regression issues. Nonetheless, it is mostly utilized to solve categorization difficulties. We believe that a random forest has trees and that more trees suggest a more effective random forest. In general, the random forest approach produces decision trees on samples of data and subsequently obtains the random forest from each one of them before selecting the best explanation. A group decision tree is better than an individual decision tree because it reduces overfitting by averaging the results. Algorithm 4 depicts the random forest classifier's mechanism.

---

#### Algorithm 4: Random Forests for Regression or Classification

---

1. For  $s = 1$  to  $T$ :
  - i. Build a bootstrap mechanism  $P$  of size  $M$  from the training database.
  - ii. Construct a random-forest tree  $F_s$  to reboot the database by iteratively recurrent the following stages for every terminal node until the smallest node size  $l_{\min}$  is obtained.
    - (a) Select  $t$  variables at random from the  $o$  variables.
    - (b) Choose the best variable/split-point among the  $t$ .
    - (c) Divide the node into two daughter nodes.

2. Outcome of the collection of trees  $\{F_s\}_1^T$ .

To achieve a prophecy at a new point  $x$ :

$$\text{Regression: } \phi_{sf}^T(x) = \frac{1}{T} \sum_{r=1}^T F_s(x).$$

Classification: Consider  $\beta_s(x)$  to be the class prophecy of the  $s^{\text{th}}$  random forest tree.

$$\beta_{sf}^T(x) = \text{majority vote } \{\beta_s(x)\}_1^T.$$

End For

---

Here  $T$  is the number of trees,  $F_s$  is the  $s^{\text{th}}$  tree and  $\beta_s$  is the class value for  $s^{\text{th}}$  tree.

For this system, the Random Forest approach, an ensemble machine learning mechanism well-known for outperforming other machine learning classifiers, was used. We applied random forest algorithms on COVID-19 sample subgroups and classified them as Normal or Pneumonia. The random forest approach uses the number of trees and the specified number of samples 100 to refine whether or not the batch prophecy is being implemented.

## 5. Result and discussion

Despite building the model, the evaluation samples achieved a loss score of about 1.9% as well as an accuracy of 98.1% in lung ultrasound images with 100 epochs. The loss rate showed a solid match between training and testing, confirming that this model is not overfitting or underfitting in the lung ultrasound picture database. Then, as shown in Fig. 5, we obtained a Receiver Operating Characteristics (ROC) curve to assess the applicability of our model. (a, b, c). An analysis of COVID-19 lung ultrasound images with non-COVID-19 and normal images revealed that this system obtains a 97% precision value as well as a 98% recall value when tested on a test set of 2110 LUS images, as shown in Table 2. Thus, we have reached the exactness of the GAN as well as the ML mechanism, which produces swift outcomes among both films of validation as well as verification samples.

The portrayal evaluations were used for identifying the Normal, COVID-19 as well as Pneumonia images that followed. Here F.N. represents False Negative, T.P. represents True Positive, F.P. represents False Positive & T.N. represents True Negative.

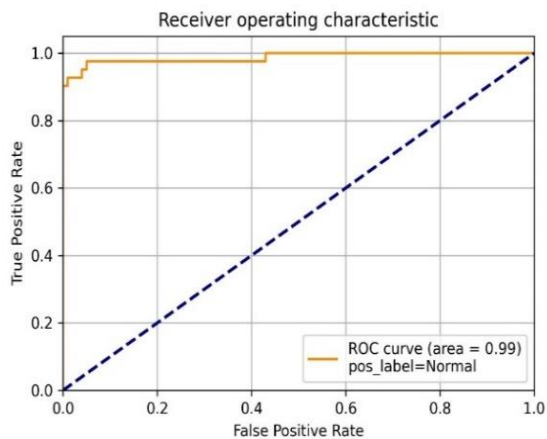
$$\text{Accuracy} = \frac{T.P.+T.N.}{T.P.+F.P.+F.N.+T.N.} \quad (10)$$

$$\text{Precision} = \frac{T.P.}{T.P.+F.P.} \quad (11)$$

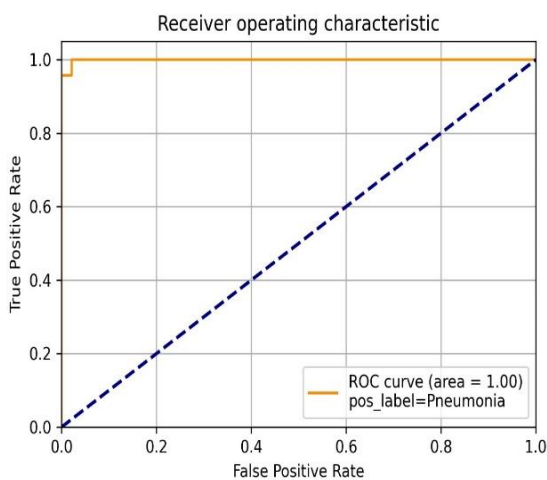
$$\text{Recall} = \frac{T.P.}{T.P.+F.N.} \quad (12)$$

$$\text{Matthews Correlation Coefficient (MCC)} = \frac{(T.P.X T.N.) - (F.P.X F.N.)}{\sqrt{(T.P.+F.P.)(T.P.+F.N.)(F.P.+T.N.)(T.N.+F.N.)}} \quad (13)$$

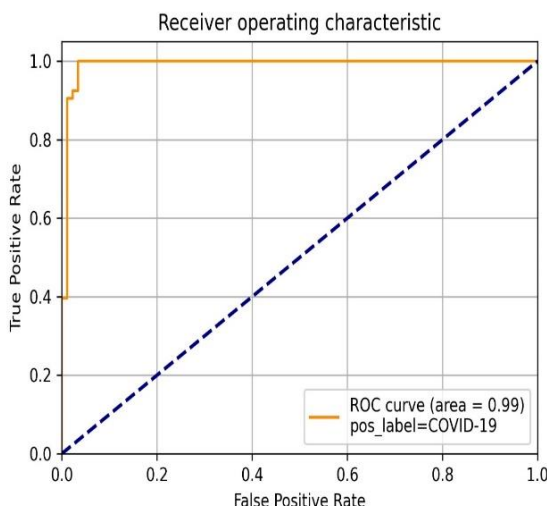
$$\text{F-Measure} = \frac{2*Precision*Recall}{Precision+Recall} \quad (14)$$



(a)



(b)



(c)

Figure. 5 Ultrasound Image Archive Efficiency: (a) The RoC graph generates 2110 test samples, with Normal as the target label, (b) The RoC graph elicits 2110 test samples, using Pneumonia as the target label, and (c) The RoC graph generates 2110 test samples, with COVID-19 serving as the target label

Table 2. Obtained performance measures for the suggested technique

Class	Recall	Precision	MCC	F-Measure
<b>Pneumonia</b>	0.98	0.98	0.97	0.98
<b>Normal</b>	0.97	0.98	0.96	0.97
<b>COVID-19</b>	0.98	0.97	0.96	0.98

Table 3. Confusion matrix for predicting verification films by pneumonia, Normal as well as COVID-19

Class	Pneu monia	Normal	COVID-19	Image count
<b>Pneumonia</b>	640	0	10	650
<b>Normal</b>	10	700	10	720
<b>COVID-19</b>	0	10	730	740
			<b>Total</b>	<b>2110</b>

The Confusion matrix for the ultrasound image collection is shown in Table 3. The accuracy and kappa values are used to compare the performance of five approaches using haralick characteristics, as shown in Table 4. The suggested GAN methodology provides better prediction than other COVID-19 and standard techniques. It demonstrates the significance of attaining such a recurrence region and indicates that such lineaments are suitable for identifying COVID-19 detection in ultrasound images. When compared to Texture, FFT, DWT, GLCM, and GLDM feature elimination approaches, the suggested model increases accuracy by 19.5%, 10.9%, 4.3%, 10.9%, and 7.6%. When COVID-19 is used as the target class, the suggested technique has a recall of 98%, an MCC of 96%, a precision of 97%, and an F-measure of 98%.

In addition, we used a variety of ML as well as DL approaches to categorize the COVID-19 data. The Random Forest approach provides great accuracy when compared to other techniques, as shown in Table 5, whereas the DL mechanism provides 84.8% accuracy in the Ultrasound picture dataset. Table 6 shows the different training and testing dividing strategies that we used. Furthermore, as indicated in Table 7, we used the cross-validation approach. When compared to the cross-validation approach and various separation ratios, the splitting distribution with 70% training set and 30% testing set produced good accuracy with a large number of images in the testing set.

Table 4. Contrast the suggested technique by five distinct techniques

Methodology	Value of Kappa	Accuracy (%)
GLDM (gm)	0.85	90.5
FFT (f)	0.8	87.2
DWT (d)	0.9	93.8
GLCM (gc)	0.8	87.2
Texture (t)	0.68	78.6
Suggested GAN model (t+f+d+gc+gm)	<b>0.96</b>	<b>98.1</b>

Table 5. Performance measures of distinct ML mechanisms on LUS films by Validation (70%) – Verification (30%) split distribution

ML Mechanisms	Accuracy (%)
Random Forest	<b>98.1</b>
Naive Bayes	51.1
Decision Tree	86.2
Logistic	93.8
SVM	46.9

Table 6. The contrast of various splits on Ultrasound films

Splits% (Train-Test)	No. of films (Train-Test)	Accuracy (%)
90 - 10	6350 – 700	98.5
80 - 20	5640 – 1410	97.1
<b>70 - 30</b>	<b>4940– 2110</b>	<b>98.1</b>
60 - 40	4230 – 2820	97.8
50 - 50	3520 – 3520	97.7

Table 7. Contrast of different folds by Cross-Validation technique by RF model

Cross-Validation	Accuracy (%)
<b>Fold - 5</b>	97.5
<b>Fold - 10</b>	98.2
<b>Avg.</b>	<b>97.9</b>

Table 8. State-of-the-art models to identify COVID-19 by Ultrasound films.

Reference	Technique	Accuracy (%)
Zhaoyu Hu et al. [35]	MCRFNet	97.7
Born et al. [34]	VGG	87.8
Gabriel et al. [30]	POCOVID-19	89
Rahimzadeh et al. [32]	NASNET Mobile	62.5
Roy et al. [36]	U-Net Deep v3+with U-net and U-net++	94 96
<b>Suggested Technique</b>	<b>GAN</b>	<b>98.1</b>

Gabriel et al.'s [30] POCVID-19 model increases classification execution by using 5-fold cross-validation. The testing results show that the proposed approach achieved 89% accuracy as well as 96% sensitivity. Jannis et al. [34] approved a VGG-positioned model with an accuracy of 87.8%. The Deep v3+ ensemble with U-net and U-net++ proposed by Roy et al. [36] improves overall performance by separating different characteristics using Xception and ResNet50V2 networks. The proposed technique had a 96% dependability. According to Rahimzadeh et al. [32], NASNET mobile has an accuracy of 62.5%. Zhaoyu Hu et al. [35] suggested an MCRFNet model that achieved 97.7% accuracy with binary classification. Table 8 depicts the many strategies used in the image collection to estimate COVID-19 persons with achievement measures probable correctness (%) for subjective research. We implemented the GAN technique in the unchanging picture database from the GitHub repository, which has been used in several recent studies. We fully utilized the machine learning process and achieved higher accuracy with balanced data than in previous studies.

## 6. Conclusion

A fictional lumen dissection of the COVID-19 diagnosis has been developed utilizing LUS images incorporating GAN, gradient mapping, as well as several haralick characteristics. Gradient visualization identifies exceptions and emphasizes crucial portions of the picture to superimpose, which are then used to fine-tune segmentation algorithms. The method is independent of any user-defined limits, making it suitable for differently ordered lung ultrasound images. Super-pixels are identified, aggregated, and separated based on surface and geographical data. The mechanism focuses on the complete design of a picture and produces comprehensive perfect results. The suggested mechanism beats POCOVID-Net, COVID-Net, and other methods by achieving best-in-class execution at a far lower cost. The method is automated and tested on a large set of 7050 images, and the results are accurate. As a result, our technique may be used to develop an effective procedure for identifying COVID-19 using LUS image dissection. With an accuracy rate of 0.97 and a recall score of 0.98, the suggested approach can identify a COVID-19-positive sample. We had a modest data size and obtained a multiclass accuracy of 98% using ultrasound images. In addition, as compared to X-rays as well as CT scans, ultrasounds are less costly, portable, easy to sterilize, non-irradiating, safe, and widely available. The results obtained are critical for quickly communicating to readers the benefits of ultrasound pictures in the context of COVID-19, as well as future tests that will deal with large databases.

## Conflicts of Interest

The authors assert that they have no conflict of interest.

## Availability of supporting data

[https://github.com/DASARINAGAVINOD/Covid-19\\_Ultrasound](https://github.com/DASARINAGAVINOD/Covid-19_Ultrasound)

## Author Contributions

DNV- Conceived the idea, Conceptualization, performed the simulation and written the manuscript. NP, JS, PKP & SM - Methodology, Writing, review and editing.

## Acknowledgments

This work is supported by Vel Tech Rangarajan Dr. Sagunthala R&D Institute of Science and Technology.

## References

- [1] H. S. Maghdid, A. T. Asaad, K. Z. Ghafoor, A. S. Sadiq, S. Mirjalili, and M. K. Khan, "Diagnosing COVID-19 pneumonia from X-ray and CT images using deep learning and transfer learning algorithms", *Multimodal image exploitation and learning*, Vol. 11734, pp. 99-110, SPIE, 2021.
- [2] H. S. Maghded, K. Z. Ghafoor, A. S. Sadiq, K. Curran, D. B. Rawat, and K. Rabie, "A novel AI-enabled framework to diagnose coronavirus COVID-19 using smartphone embedded sensors: design study", In: *Proc. of 2020 IEEE 21st International Conf. on Information Reuse and Integration for Data Science (IRI)*, Las Vegas, NV, USA, pp. 180-187, 2020.
- [3] A. M. Ali, K. Ghafoor, A. Mulahuwaih, and H. Maghdid, "COVID-19 pneumonia level detection using deep learning algorithm and transfer learning", *Evolutionary Intelligence*, Vol. 17 No. 2, pp. 1035-1046, 2024.
- [4] S. Shah, A. Mulahuwaih, K. Z. Ghafoor, and H. S. Maghdid, "Prediction of global spread of COVID-19 pandemic: a review and research challenges", *Artificial Intelligence Review*, Vol. 55, pp. 1607-1628, 2022.
- [5] D. Dong, Z. Tang, S. Wang, H. Hui, L. Gong, Y. Lu, and H. Li, "The role of imaging in the detection and management of COVID-19: a review", *IEEE Reviews in Biomedical Engineering*, Vol. 14, pp. 16-29, 2020.
- [6] J. E. Bourcier, J. Paquet, M. Seinger, E. Gallard, J. P. Redonnet, F. Cheddadi, D. Garnier, J. M. Bourgeois, and T. Geeraerts, "Performance comparison of lung ultrasound and chest x-ray for the diagnosis of pneumonia in the ED", *Am. J. Emerg. Med.*, Vol. 32, pp. 115-118, 2014.
- [7] Y. Fang, H. Zhang, J. Xie, M. Lin, L. Ying, P. Pang, and W. Ji, "Sensitivity of chest CT for COVID-19: Comparison to RT-PCR", *Radiology*, Vol. 296, pp. 115-117, 2020.
- [8] Y. Yang, Y. Huang, F. Gao, L. Yuan, and Z. Wang, "Lung ultrasonography versus chest CT in COVID-19 pneumonia: A two-centered retrospective comparison study from China", *Intensive Care Med*, Vol. 46, pp. 1761-1763, 2020.
- [9] N. Chen, M. Zhou, X. Dong, J. Qu, F. Gong, Y. Han, Y. Qiu, J. Wang, Y. Liu, and Y. Wei, "Epidemiological and clinical characteristics of 99 cases of 2019 novel coronavirus pneumonia in wuhan, china: a descriptive study", *The Lancet*, Vol. 395, pp. 507-513, 2020.

- [10] C. Bao, X. Liu, H. Zhang, Y. Li, and J. Liu, "COVID-19 computed tomography findings: a systematic review and meta-analysis", *J Am Coll Radiol*, Vol. 17, No. 6, pp. 701-709, 2020.
- [11] E. Y. Lee, M. Y. Ng, and P. L. Khong, "COVID-19 pneumonia: what has ct taught us?", *The Lancet Infectious Diseases*, Vol. 20, No. 4, pp. 384-385, 2020.
- [12] D. Buonsenso, D. Pata, and A. Chiaretti, "COVID-19 outbreak: less stethoscope, more ultrasound", *The Lancet Respiratory Medicine*, Vol. 8, No. 5, pp. e27, 2020.
- [13] Kanne, and P. Jeffrey, "Chest CT findings in 2019 novel coronavirus (2019-nCoV) infections from Wuhan, China: key points for the radiologist", *Radiology*, Vol. 295, No. 1, 2020.
- [14] F. Mojoli, B. Bouhemad, S. Mongodi, and D. Lichtenstein, "Lung ultrasound for critically ill patients", *Amer. J. Respiratory Crit. Care Med*, Vol. 199, pp. 701-714, 2019.
- [15] R. Raheja, M. Brahmavar, D. Joshi, and D. Raman, "Application of lung ultrasound in critical care setting: A review", *Cureus*, Vol. 11, No. 7, pp. e5233, 2019.
- [16] Y. Amaty, J. Rupp, F. M. Russell, J. Saunders, B. Bales, and D. R. House, "Diagnostic use of lung ultrasound compared to chest radiograph for suspected pneumonia in a resource-limited setting", *Int. J. Emergency Med*, Vol. 11, No. 1, pp. 8, 2018.
- [17] E. Poggiali, "Can lung US help critical care clinicians in the early diagnosis of novel coronavirus (COVID-19) pneumonia?", *Radiology*, Vol. 295, No. 3, 2020.
- [18] Q. Y. Peng, Chinese Critical Care Ultrasound Study Group, X. T. Wang, and L. N. Zhang, "Findings of lung ultrasonography of novel corona virus pneumonia during the 2019-2020 epidemic", *Intensive Care Med*, Vol. 46, No. 5, pp. 849-850, 2020.
- [19] G. Soldati, A. Smargiassi, R. Inchingolo, D. Buonsenso, T. Perrone, D. F. Briganti, S. Perlini, E. Torri, A. Mariani, E. E. Mossolani, and F. Tursi, "Is there a role for lung ultrasound during the COVID-19 pandemic?", *Journal of Ultrasound in Medicine*, Vol. 39, No. 7, pp.1459, 2020.
- [20] G. Soldati, A. Smargiassi, R. Inchingolo, D. Buonsenso, T. Perrone, D. F. Briganti, S. Perlini, E. Torri, A. Mariani, E. E. Mossolani, and F. Tursi, "Proposal for international standardization of the use of lung ultrasound for patients with COVID-19: a simple, quantitative, reproducible method", *Journal of Ultrasound in Medicine*, Vol. 39, No. 7, pp.1413-1419, 2020.
- [21] K. Stefanidis, S. Dimopoulos, E. S. Tripodaki, K. Vitzilaios, P. Politis, P. Piperopoulos, and S. Nanas, "Lung sonography and recruitment in patients with early acute respiratory distress syndrome: a pilot study", *Critical Care*, Vol. 15, pp.1-8, 2011.
- [22] K. A. Stewart, S. M. Navarro, S. Kambala, G. Tan, R. Poondla, S. Lederman, K. Barbour, and C. Lavy, "Trends in ultrasound use in low- and middle-income countries: a systematic review", *International Journal of Maternal and Child Health and AIDS*, Vol. 9, No. 1, pp.103, 2020.
- [23] L. Tutino, G. Cianchi, F. Barbani, S. Batacchi, R. Cammelli, and A. Peris, "Time needed to achieve completeness and accuracy in bedside lung ultrasound reporting in intensive care unit", *Scandin. J. Trauma, Resuscitation Emergency Med.*, Vol. 18, No. 1, pp. 44, 2010.
- [24] L. Long, H. T. Zhao, and Z. Y. Zhang, "Lung ultrasound for the diagnosis of pneumonia in adults: a meta-analysis", *Medicine*, Vol. 96, pp. e5713, 2017.
- [25] D. A. Lichtenstein, and G. A. Mezière, "Relevance of lung ultrasound in the diagnosis of acute respiratory failure: the blue protocol", *Chest*, Vol. 134, pp. 117-25, 2018.
- [26] O. J. Ma, and J. R. Mateer "Trauma ultrasound examination versus chest radiography in the detection of hemothorax", *Ann Emerg Med*, Vol. 29, pp. 312, 1997.
- [27] D. Buonsenso, D. Pata, and A. Chiaretti, "COVID-19 outbreak: less stethoscope, more ultrasound.", *Lancet Respir Med*, Vol. 8, pp. e27, 2020.
- [28] C. F. Dietrich, G. Mathis, and M. Blaivas, "Lung B-line artefacts and their use", *J Thorac Dis*, Vol. 8, pp. 1356, 2016.
- [29] D. N. Vinod, and S. R. S. Prabakaran, "Data science and the role of Artificial Intelligence in achieving the fast diagnosis of COVID-19", *Chaos, Solitons & Fractals*, Vol. 140, p. 110182, 2020.
- [30] J. Born, G. Brändle, M. Cossio, M. Disdier, J. Goulet, J. Roulin, and N. Wiedemann, "POCOVID-Net: automatic detection of COVID-19 from a new lung ultrasound imaging dataset (POCUS)", *ArXiv Preprint*, arXiv:2004.12084, 2020.
- [31] K. Simonyan, and A. Zisserman, "Very deep convolutional networks for large-scale image recognition", *ArXiv Preprint*, arXiv:1409.1556, 2014.
- [32] N. Srivastava, G. Hinton, A. Krizhevsky, I. Sutskever, and R. Salakhutdinov, "Dropout: a simple way to prevent neural networks from

- overfitting”, *The Journal of Machine Learning Research*, Vol. 15, No. 1, pp. 1929-1958, 2014.
- [33] S. Ioffe, and C. Szegedy, “Batch normalization: Accelerating deep network training by reducing internal covariate shift”, *ArXiv Preprint*, arXiv:1502.03167, 2015.
- [34] J. Born, N. Wiedemann, M. Cossio, C. Buhre, G. Brändle, K. Leidermann, and K. Borgwardt, “Accelerating Detection of Lung Pathologies with Explainable Ultrasound Image Analysis”, *Applied Sciences*, Vol. 11, No. 2, pp. 672, 2021.
- [35] Z. Hu, Z. Liu, Y. Dong, J. Liu, B. Huang, A. Liu, and J. Zhou, “Evaluation of lung involvement in COVID-19 pneumonia based on ultrasound images”, *BioMedical Engineering OnLine*, Vol. 20, No. 1, pp. 1-15, 2021.
- [36] S. Roy, W. Menapace, S. Oei, B. Luijten, E. Fini, C. Saltori, and L. Demi, “Deep learning for classification and localization of COVID-19 markers in point-of-care lung ultrasound”, *IEEE Transactions on Medical Imaging*, Vol. 39, No. 8, pp. 2676-2687, 2021.
- [37] B. Zhou, A. Khosla, A. Lapedriza, A. Oliva, and A. Torralba, “Learning deep features for discriminative localization”, In: *Proc. of the IEEE Conf. on Computer Vision and Pattern Recognition*, Las Vegas, NV, USA, pp. 2921-2929, 2016.
- [38] R. R. Selvaraju, M. Cogswell, A. Das, R. Vedantam, D. Parikh, and D. Batra, “Grad-cam: Visual explanations from deep networks via gradient-based localization”, In: *Proc. of the IEEE International Conf. on Computer Vision*, Venice, Italy, pp. 618-626, 2017.
- [39] A. Z. Khuzani, M. Heidari, and S. A. Shariati, “COVID-Classifer: An automated machine learning model to assist in the diagnosis of COVID-19 infection in chest x-ray images”, *Scientific Reports*, Vol. 11, No 1, pp. 1-6, 2021.
- [40] K. Sahinbas, and F. O. Catak, “Transfer learning-based convolutional neural network for COVID-19 detection with X-ray images”, In *Data Science for COVID-19*, Academic Press, pp. 451-466, 2020.
- [41] F. O. Catak, and K. Şahinbaş, “Human-in-the-Loop Enhanced COVID-19 Detection in Transfer Learning-Based CNN Models”, In *Computational Intelligence for COVID-19 and Future Pandemics*, Springer, Singapore, pp. 71-87, 2021.
- [42] Y. Li, and L. Xia, “Coronavirus disease 2019 (COVID-19): role of chest CT in diagnosis and management”, *Ajr Am J Roentgenol*, Vol. 214, No. 6, pp. 1280-1286, 2020.
- [43] D. N. Vinod, and S. R. S. Prabaharan, “Elucidation of infection asperity of CT scan images of COVID-19 positive cases: A Machine Learning perspective”, *Scientific African*, Vol. 20, pp. e01681, 2023.